We are IntechOpen,
the world's leading publisher of
Open Access books
Built by scientists, for scientists

4,800
Open access books available

122,000
International authors and editors

135M
Downloads

Our authors are among the

154
Countries delivered to

TOP 1%
most cited scientists

12.2%
Contributors from top 500 universities

CLARIVATE ANALYTICS
BOOK CITATION INDEX
INDEXED

WEB OF SCIENCE™

Selection of our books indexed in the Book Citation Index
in Web of Science™ Core Collection (BKCI)

Interested in publishing with us?
Contact book.department@intechopen.com

Numbers displayed above are based on latest data collected.
For more information visit www.intechopen.com

Silicon Carbide for Novel Quantum Technology Devices

Stefania Castelletto, Lorenzo Rosa and
Brett C. Johnson

Additional information is available at the end of the chapter

Abstract

Silicon carbide (SiC) has recently been investigated as an alternative material to host deep optically active defects suitable for optical and spin quantum bits. This material presents a unique opportunity to realise more advanced quantum-based devices and sensors than currently possible. We will summarise key results revealing the role that defects have played in enabling optical and spin quantum measurements in this material such as single photon emission and optical spin control. The great advantage of SiC lies in its existing and well-developed device processing protocols and the possibilities to integrate these defects in a straightforward manner. There is particular current interest in nanomaterials and nanophotonics in SiC that could, once realised, introduce a new platform for quantum nanophotonics and in general for photonics. We will summarise SiC nanostructures exhibiting optical emission due to multiple polytypic bandgap engineering and deep defects. The combination of nanostructures and in-built paramagnetic defects in SiC could pave the way for future single-particle and single-defect quantum devices and related biomedical sensors with single-molecule sensitivity. We will review relevant classical devices in SiC (photonics crystal cavities, microdiscs) integrated with intrinsic defects. Finally, we will provide an outlook on future sensors that could arise from the integration of paramagnetic defects in SiC nanostructures and devices.

Keywords: Silicon carbide deep defects, Paramagnetic properties, Optical-detected magnetic resonance, Single-photon sources

1. Introduction

The most common and technologically advanced SiC polytypes are 4H-SiC and 6H-SiC with hexagonal structures and 3C-SiC with a zinc-blende crystal structure (cubic). High-quality

INTECH
open science | open minds

bulk single-crystal 3C-SiC can be grown epitaxially on different substrates, most notably on silicon. This has led to many exciting devices fabricated with this particular polytype[1]. SiC has a wide bandgap (2.4-3.2 eV depending on the polytype), a high thermal conductivity, the ability to sustain high electric fields before breakdown and the highest maximum current density, making it ideal for high-power electronics [2]. More recently, it has become a notable material in the field of quantum computing and spintronics as several of its intrinsic defects are associated with an electron spin that can be used as quantum bit [3, 4]. To enhance solid-state quantum systems scalability, a fully integrated device with quantum control should be built; thus, quantum systems should be part of the material used to fabricate the final device. Other solid-state quantum systems fully integrated into a functional device[5–7] operate at cryogenic temperatures (4 K or below), limiting their engineering and scalability. A room temperature solid-state "qubit" is the nitrogen vacancy (NV) centre[8] in diamond; yet diamond is not mature for standard device fabrication protocols. SiC, on the other hand, is widely used in LEDs (commonly as a substrate for GaN films), power electronics and microelectromechanical and nano-electromechanical systems (MEMs, NEMs) [9, 10] and has well-developed device processing protocols which are compatible with industry standards. In addition, nanostructures can be formed in SiC such as nanoparticles, quantum dots, nanowires and nanopillars. The ability to grow SiC on silicon provides an unprecedented advantage which facilitates the fabrication of nanophotonic cavities[11, 12]. As a compound semiconductor, SiC harbours a rich assortment of optically active intrinsic and extrinsic defects that can be used as quantum systems.

In this chapter, we will summarise key findings and the main properties of deep optical and paramagnetic defects in bulk SiC that very recently have prompted novel quantum effects such as single-photon source (SPS) and quantum coherence control of their spin[13–17]. We will review defects with optical emission used in quantum spintronics and quantum optics, optically detected resonance methods applied to these defects, the achievement of coherent control of ensemble and single spins and their present spin coherence times. We will review single-photon emission from nanostructures of silicon carbide[18, 19]. We will review recent nanophotonics advances[20–30] in this material to achieve defect integration and enhancement. Other applications of the engineered defects in quantum technologies are also summarised. Some challenges still remain before this material can fully realise its potential in advancing quantum technology. In the summary, we critically analyse present challenges based on the reported results and provide an outlook of likely future investigations that can lead to successful application of SiC for quantum devices.

2. Deep defects in SiC with quantum properties

Many deep-energy-level defects within the bandgap give rise to radiative recombination in SiC with photoluminescence (PL) from the UV to the infrared. The dual compound nature and the existence of nonequivalent lattice sites in different polytypes (quasi-cubic, k, and hexagonal, h) give rise to a large variety of possible PL. Here, we will discuss only recently investigated defects that provided so far experimental evidence of quantum effects[14–16]. These defects are intrinsic defects, known as silicon vacancies (V_{Si})[31–33], divacancies ($V_{Si}V_C$)[34] and carbon antisite-vacancy pair ($C_{Si}V_C$)[35, 36]. In Figures 1-3, we show the atomistic defect structure and the presently understood energy levels corresponding to so far identified quantum systems in 4H, 6H and 3C polytypes. These defects coincide with

the most commonly previously observed intrinsic defects in the material. They can be created in ensemble by neutron or electron irradiation, followed by annealing, as well as they can be created during growth. Recent experimental challenges rely in their creation as isolated systems or individual defects with their correlation to the ensemble level for their identification in bulk SiC. For this to be reliable, due to the large variability properties of the bulk material, which also can present many defects at the same time, the purity of the pristine wafer resulted to be essential. Therefore, the isolation of single defects as quantum systems was performed in high purity 4H intrinsic SiC. These defects act as radiative recombination centres within the bandgap with a PL achieved by out-of-resonance excitation with a laser. The PL is typically characterised by a sharp zero-phonon line (ZPL) and phonon side bands (PSB) at longer emission wavelengths. Recombination centres are modelled as a quantum system with ground, excited and metastable states (a two- or three-level system). These defects can have different ZPLs in the first instance according to the polytype, which provides nonequivalent crystallographic sites in the matrix. Additionally, the material doping can influence the emission wavelength. They are often characterised by a charge state which also can influence the spectral location of the ZPL peak. The charge state is also associated to the spin state (mostly of the ground state) of the defect, which can be observed from PL measurements as a reduction/enhancement (depending on the mechanism of the population of the energy levels) of the PL, when probed with the application of an additional magnetic field or a microwave excitation in resonance with the spin sublevels. Other defects also yielding quantum properties are not yet presently completely identified. The main effect on the variation of the defects ZPLs is related to the polytype, whether the defect occupies an axial position in the lattice (orientation along the c-axis, hh or kk lattice location) or an off-axis position (hk, kh orientation basal); thus, at least 2^n ZPLs can be present for n-nonequivalent crystallographic site positions. In addition, the symmetry of the defects can give rise to other ZPLs with an excited state split by Jahn-Teller distortion, reducing the symmetry and introducing additional ZPLs. V_{Si} consists of a missing silicon atom in the matrix. In 4H-SiC, V_{Si} shows two ZPLs (two nonequivalent sites) stable up to 500-600°C; in addition, two possible charge states are known. The ZPL, known as V_1, emits at 862.2 nm, while V_2 emits at 917.0 nm. These lines have been associated to a negative charge state, while the neutral charge state has ZPLs at 859.0 nm and 861.7 nm, respectively. Both defects are quite common in 4H- and 6H-SiC, as well as in 3C. The V_{Si} negative charge in 4H and 6H has a high spin (S=3/2) ground state, shown in Figure 1(c)[32]. V_{Si} ZPL emissions in 6H-SiC are known as V_1, V_2 and V_3 lines, owning to the three nonequivalent sites (h,k_1,k_2; see Figure 1) at 865 nm, 887 nm and 906 nm, respectively.

The closest pair of V_{Si} and carbon vacancy V_C, the divacancy $V_{Si}V_C$, can form during the migration of the isolated vacancies. PL arising from $V_{Si}V_C$ is attributed to its neutral charge state ($V_{Si}V_C^0$) and has several ZPLs in 4H- and 6H-SiC. In 4H-SiC, the $V_{Si}V_C$ defects possess four ZPLs (stable up to 1,500°C) associated to specific PL at 997.5 nm, 1013.6 nm, 1050.7 nm and 1053.9 nm. These ZPLs are related the axial (hh, kk) and basal (hk, kh) location in the lattice (see Figure 2). Other ZPLs in a similar wavelength range have been recently found [38] denominated PL5 (1043 nm) and PL6 (1039 nm) due to their unknown origin. In 6H-SiC, the $V_{Si}V_C$-defect-known ZPLs are at 998.7nm, 1010.9 nm, 1030 nm, 1048.7 nm and 1074.6nm. ZPLs obtained in irradiated 6H samples at 1,139 nm; 1,135 nm; 1,124 nm; 1,108 nm; and 1,093 nm were found to have quantum characteristics similar to the ($V_{Si}V_C^0$)[39] and were associated with UD2 defect, previously known in 4H- and 6H-SiC[40, 41].
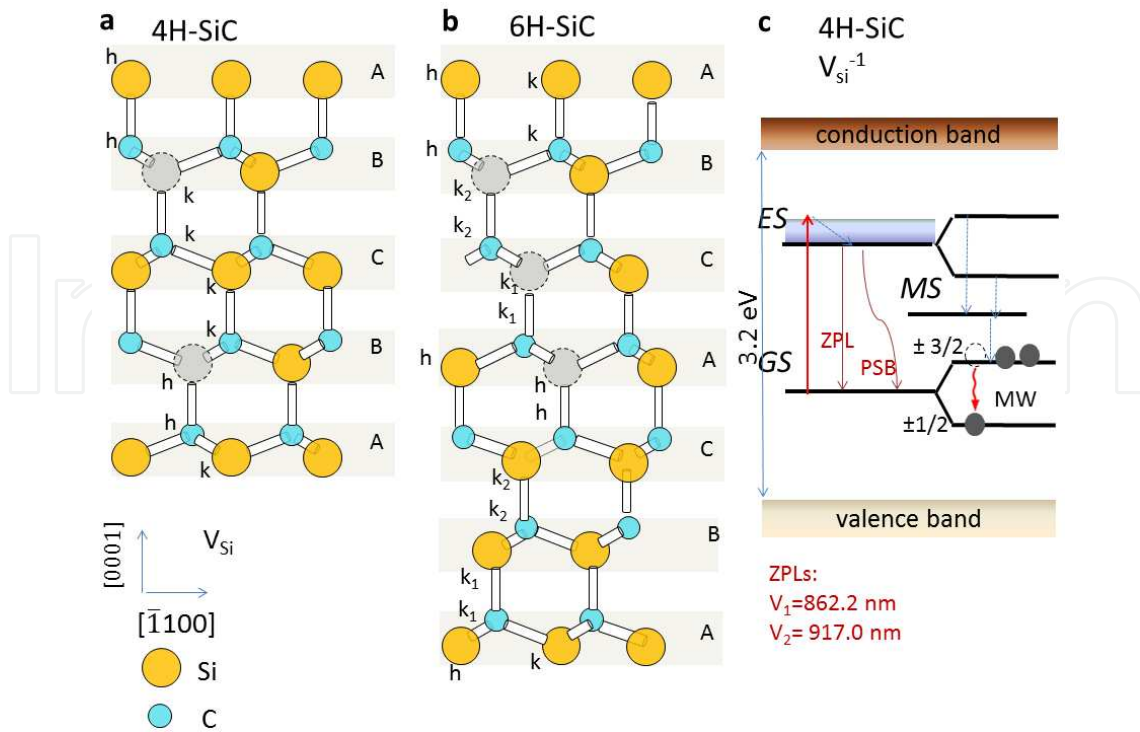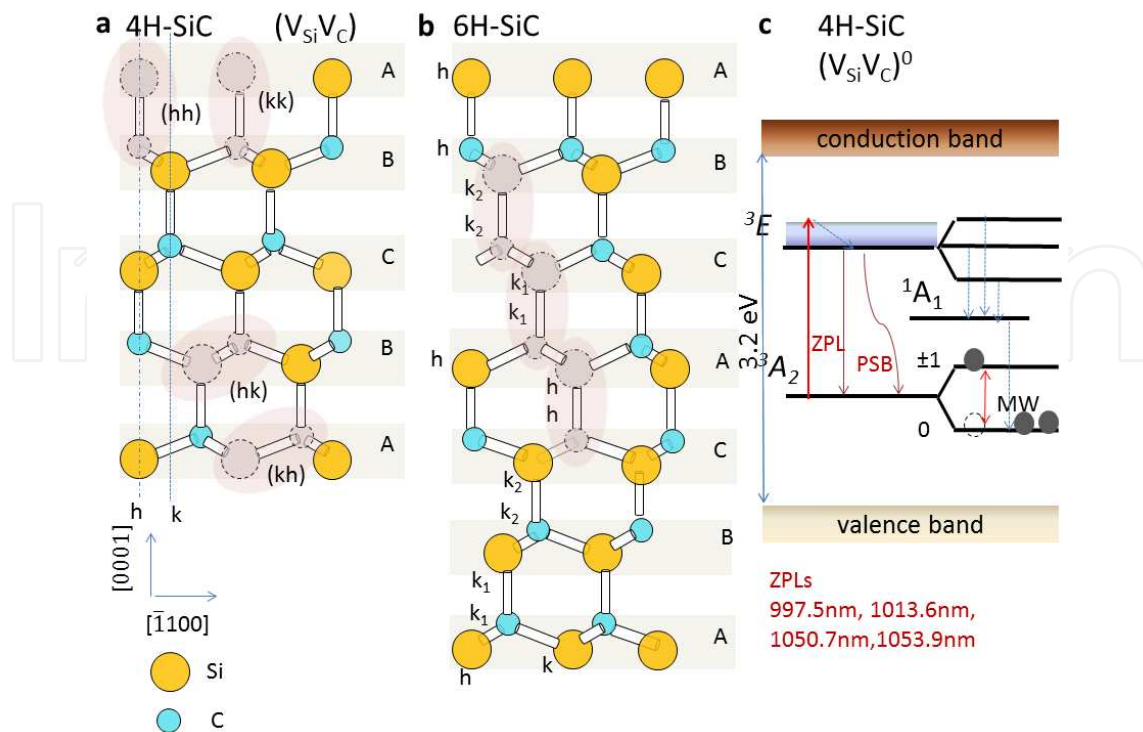
Figure 1. Representation of the atomic structure of the V_{Si} in the SiC lattice in **a** 4H and **b** 6H polytypes, located in different nonequivalent sites (k,h in 4H) and (h, k_1,k_2 in 6H). **c** Visualisation of the energy levels in the negatively charged state of the V_{Si} for 4H, where the ground state (GS), excited state (ES) and metastable state (MS) structures are visualised, with the ZPL, PSB and spin level of the high spin S=3/2 ground state. A microwave transition in the GS is responsible for the PL enhancement of the ZPL in the presence of a microwave excitation (MW). Both 4H and 6H polytypes containing these defects have been used for quantum control of the ground state spin[16, 37]

In a dual element semiconductor, the antisite-vacancy complex is an intrinsic defect. The defect possesses C_{3v} symmetry if C_{Si} is along the c-axis (on-axis configurations, $C_{Si}V_C$(kk) and $C_{Si}V_C$(hh)), while it has C_{1h} symmetry if C_{Si} is out of the c-axis (off-axis configurations, $C_{Si}V_C$(kh) and $C_{Si}V_C$(hk)) in 4H-SiC (see Figure 3**a**). Its PL was found to be in the 648-678 nm range and initially attributed to its neutral charge state[36]. It has been known as AB lines found in both 4H- and 6H-SiC with also different doping. According to recent modelling, the neutral charged state of the $C_{Si}V_C$ defect associated to the AB lines should not have any visible PL; therefore, the visible PL is attributed to the positive charge state of this defect with S=1/2. Eight ZPLs were associated with the $C_{Si}V_C$ in 4H-SiC, labelled as A_1 = 648.7 nm, A_2 =651.8 nm, A_3 = 665.1 nm, A_4=668.5 nm, B_1 = 671.7 nm, B_2 =673.0 nm, B_3 =675.2 nm and B_4 = 676.5 nm. The eight AB PL lines in 4H-SiC can naturally account for the four ground-state configurations (hh, kk, hk, kh) where each possesses two ZPLs due to the splitting of the excited state.

## 3. Single-photon source in bulk material

Over the past decade, single-photon generation has been observed in many physical systems such as single molecules[42], quantum dots[43, 44], diamond colour centres[45] and others[46, 47]. The generation and detection of single photons play a central role in the foundation of quantum mechanics. Additionally, an efficient and high-quality single-photon

Figure 2. Representation of the atomic structure of the $V_{Si}V_C$ in the SiC lattice in **a** 4H and **b** 6H polytypes, located in different nonequivalent sites (k, h in 4H) and (h, k_1, k_2 in 6H).**c** Visualisation of the energy levels in the neutral state of the $(V_{Si}V_C^0)$ for 4H, where the ground state ($^3A_2$), excited state (^3E) and metastable state ($^1A_1$) structures are visualised, with the ZPL, PBS and spin level of the high spin S=1 ground state. A microwave transition in the GS is responsible for the PL enhancement of the ZPL in presence of a microwave excitation (MW). Both 4H and 6H polytypes containing these defects have been used for quantum control of the ground state spin [15, 38, 39]
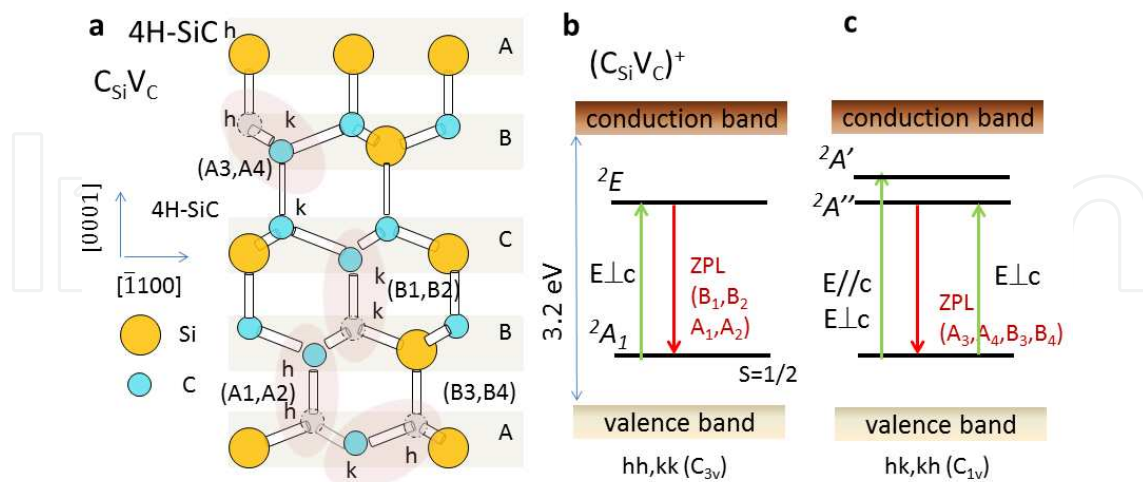

Figure 3. Representation of the atomic structure of the $C_{Si}V_C$ in the SiC lattice in **a** 4H, located in different nonequivalent sites (k, h in 4H). Visualisation of the energy levels in the positive charge state of the $(C_{Si}V_C^+)$ for 4H, where the ground state ($^2A_1$) and excited state (^2E) are visualised, with the ZPLs in the axial **b** and basal **c** defects position [14]
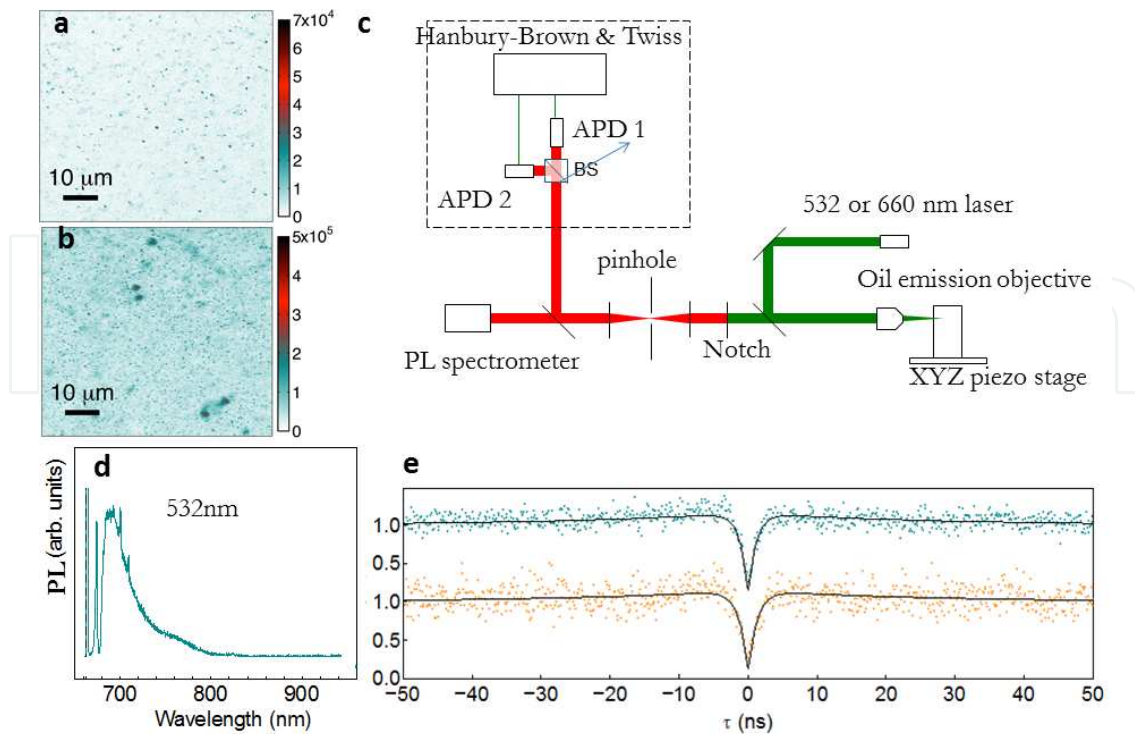
Figure 4. Confocal maps of **a** untreated sample that occasionally shows native defects whose origin is yet unclear and **b** confocal map showing irradiated generated single defects with a low temperature annealing of 300 °C. The colour code indicates much brighter emitters in the irradiated samples. **c** Experimental set-up.**d** Typical room temperature PL of the SPS. **e** Photon correlation of two SPSs in the irradiated sample excited at 532 and 660 nm. The reduction of photon coincidence at zero delay time below 0.5 indicates the presence of single-photon statistics

source operating at room temperature is needed to ensure secure communication channels via the implementation of protocols of quantum key distribution. SPSs are needed to establish quantum photonics communication networks[48]. At the present, SiC has provided in bulk materials SPS from all the defects discussed in Section 1, isolated in ultrapure 4H-SiC. The first observation of single-photon statistics from SiC was associated with the PL from a single C antisite-vacancy pair. This defect is the brightest single-photon emitter in a bulk solid state system operating at room temperature, showing up to 10^6 counts/s at saturation, indicating a high quantum efficiency and occurring in the region 650-700 nm. The single-photon emission corresponds to a 3-level atomic system, due to the presence of a metastable state. The brightness is associated to the polarisation selection rules of these defects, most of the time parallel to the excitation electric field, as well as to the dipole strength (short radiative lifetime of 1.5 ns). The defect has been isolated using confocal microscopy in electron-irradiated high-purity, semi-insulating (HPSI) SiC along the main axis (1,000) from a 3-inch wafer, containing $V_C \sim 10^{14}/cm^3$, $B \sim 10^{14}/cm^3$, N and other defects$< 10^{14}/cm^3$. Electron irradiation with energy of 2Mev was used to create defects deeper in the material, and fluences of 10^{13}-$10^{14}cm^{-3}$ were used for the single-defect creation. In Figure 4, the confocal maps, experimental set-up, typical PL and photon correlation measured using a Hanbury Brown and Twiss interferometer indicate SPS. PL at room temperature in single emitters was compared to ensemble generated with electron fluences of $10^{17}cm^{-3}$, showing high similarity when excited at 532 nm.
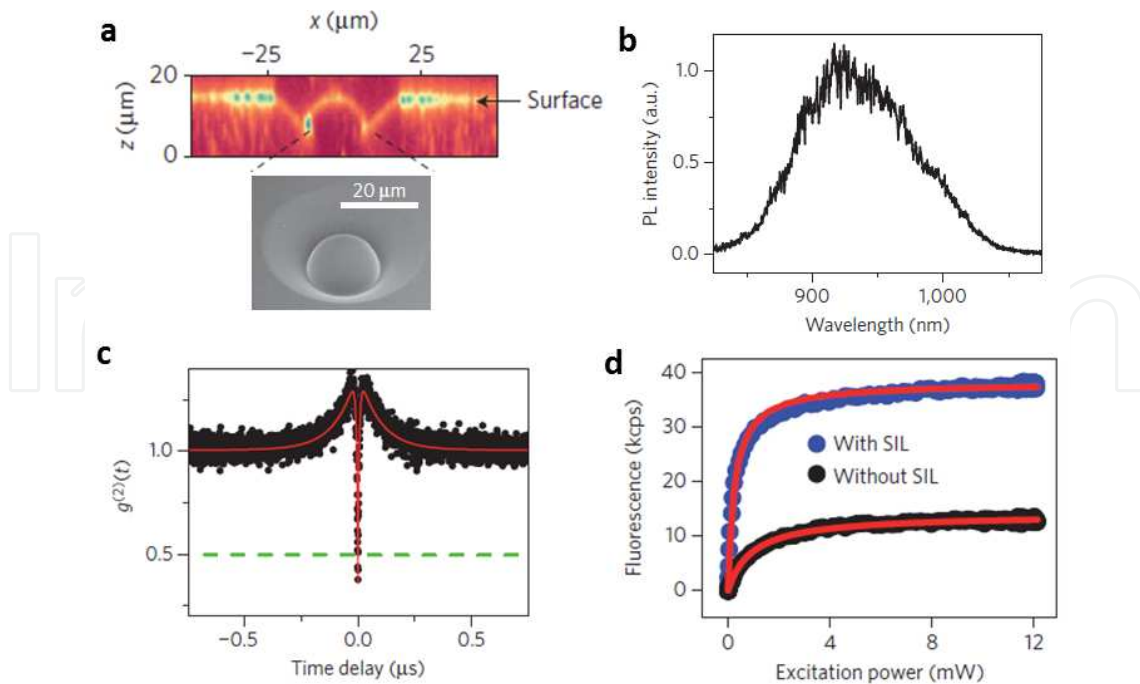
Figure 5. Confocal map of **a** a solid immersion lens (SIL) containing a single V_{Si} defect and the SIL SEM image. **b** PL at room temperature of the V_{Si}. **c** Photon correlation of defect PL in the irradiated sample. The reduction of photon coincidence at zero delay time below 0.5 indicates the presence of single-photon statistic. **d** Photon count rate from a single defect versus excitation power with and without the SIL. Images reproduced with permission from Macmillan Publishers Ltd: Nature Materials [16], copyright (2015)

V_{Si} denoted as V_2 lines with ZPL at 917 nm in bulk 4H-SiC has also been isolated [16], using confocal microscopy exciting the substrate by a 730 nm laser. The defect at the single level was created by electron irradiation and low-temperature annealing in vacuum. Due to the geometry of the defect location in the material cut along (1,000) axis, this defect could not be excited with the laser polarisation along to the defect axis, yielding a very low count rate at the single-photon level (15,000counts/s) at saturation. A solid immersion lens of 20 μm diameter was milled using a Ga focussed ion beam in the material to increase the collection efficiency of the single photons, proving an enhancement of a 2.5 factor. Similar results are shown of isolation of this defect in 4H by [17]; in this case, the defect was created using neutron irradiation, and a clear increase of the number of defects with radiation fluences was observed. Similar count rate and PL broad emission in the 900 nm region was observed for the single emitter. A lifetime of 6.1 ns was determined and perfect photo-stability was observed. In Figure 5, we show the main properties of this defect as a SPS.

Divacancies were also isolated from 120 μm 4H-SiC single-crystal epitaxial film grown on an n-type 4H-SiC substrate. The substrate was grown by hotwall chemical vapour deposition, a technique used to create commercial quality, multilayer electronic structures at the wafer scale. The epilayer is optimised to have no basal plane dislocations or polytype inclusions and a very low (5 $10^{13} cm^{-3}$) unintentional dopant density. The epilayer was mechanically separated from the substrate, polished and diced and then irradiated with 2 MeV electrons at a range of fluences 5 $\times 10^{12} cm^{-2}$ to $10^{15} cm^{-2}$. Annealing was used to achieve the migration of the vacancy to form the defects. Superconducting nanowire-based single-photon detectors able to detect the infrared emission were integrated into a home-built confocal microscope.
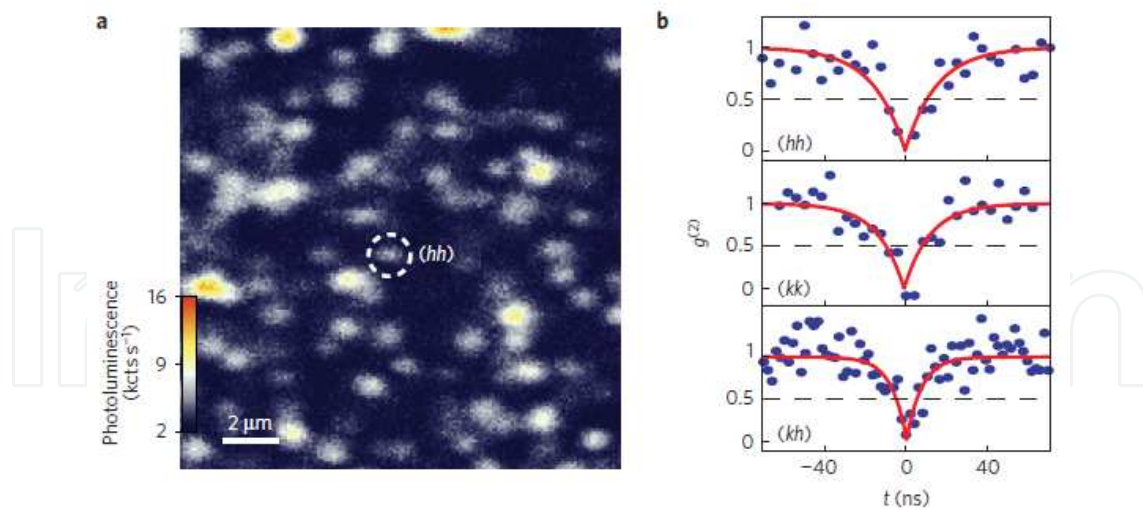
Figure 6. Confocal map of **a** a 4H-SiC membrane irradiated at 10^{13} cm^{-3} electron fluence. PL is collected by a confocal at a depth of 20 μm at a temperature of 20 K. PL spots were mostly identified as divacancies, though not all bright spots correspond to isolated single defects. **b** Photo-correlation $g^{(2)}(\tau)$ measurements for single divacancy defects located corresponding to (hh), (kk) and (kh) sites. Fits to a simple two-level model are shown. Images reproduced with permission from Macmillan Publishers Ltd: Nature Materials [15], Copyright (2015)

Excitation was performed with 975 nm continuous-wave laser. The sample was cooled to 20 K to observe distinct bright spots in a scanning PL image, as shown in Figure 6. The optical lifetimes of the neutral divacancies is 14±3 ns. The measured count rates were very low in the range of 3000-5000 counts/s, due to detector losses ($\sim$ 28% detection efficiency) in the spectral region of their ZPLs and the low collection efficiency from low NA objective in the cryostat. In addition, because of a high background due to polishing artifacts it was required to focus deep (20 μm) below the SiC surface to observe isolated single emitters, which added another 20-30% optical losses.

4. Single-photon sources in nanomaterials

SiC nanomaterial scientific interest is motivated by the material larger potentials at the nanoscale in optoelectronics as an efficient ultraviolet emitter. SiC nanomaterial has also generated interest for its biocompatibility in nanomedicine or as emitting nanoprobes for imaging[49–51]. PL spectra of SiC nanostructures and nanopowder have been largely studied. The most common PL origin due to subgap emission is radiative recombination of defects and surface states[52], while above-gap emission is attributed to quantum confinement phenomenon in small nanocrystals such as quantum dots (QDs). At present the peak emission wavelengths of the SiC QDs are in the UV-blue-green region, typically between 380 nm and 550 nm[53–56]. This spectral emission region, however, is not ideal for biomedical applications due to the cell autofluorescence in the same spectral band. Additionally, infrared would be desirable for in-depth biological tissue imaging.

Recently the first demonstration of a deep defect within the bandgap has been shown in SiC nanocrystals obtained from 3C polytype[18], showing an emission in the red spectral region (650 nm). This red emission has been demonstrated to emit single photons. Two sources of SiC nanoparticles were explored: commercial 3C SiC nanomaterial with an average
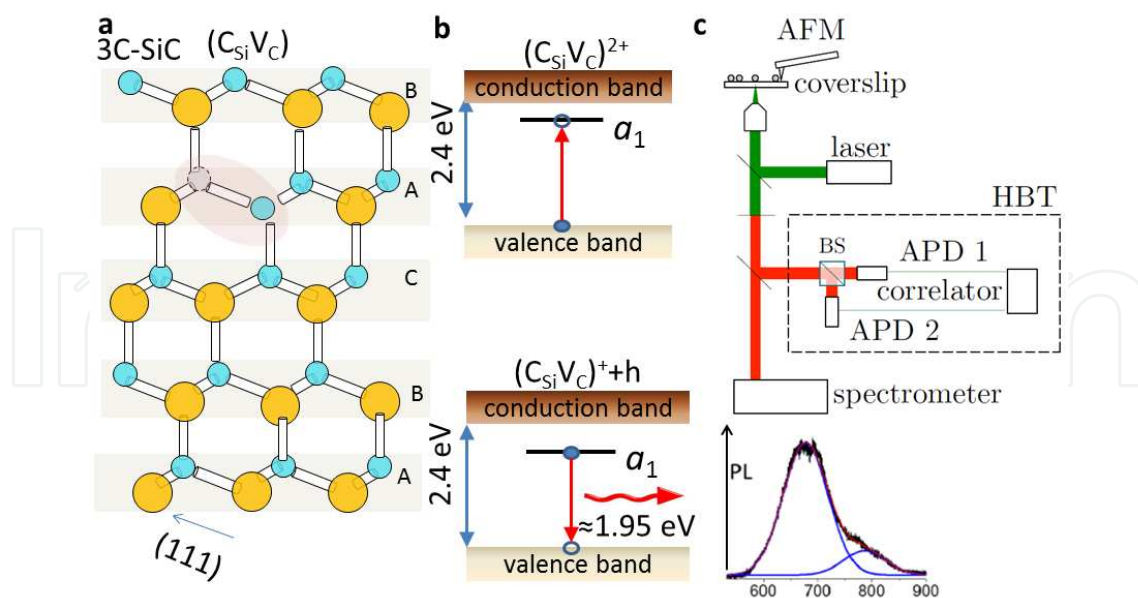
Figure 7. Representation of the atomic structure of the $C_{Si}V_C$ in the 3C-SiC lattice in **a**. **b** Visualisation of the energy levels in the double-positive charge state of the ($C_{Si}V_C^{2+}$) for 3C, where the ground state and excited state are visualised. The defect ZPL is around 648 nm from ensemble measurements (not clearly observed at the single level at room temperature).**c** Experimental set-up used to study the 3C-SiC nanoparticle defect SPS and room temperature PL measured from SPS [18]

size of 45 nm suspended in ethanol and large (size: 200-500nm) in-house synthesised SiC nanocrystals suspended in MilliQ, dried on glass cover slip[57]. A room temperature custom-built confocal microscope combined with an atomic force microscope (Figure 7**c**) was used to correlate the size of the nanocrystals with PL, while photon correlation was used to determine the quantum properties of the PL. Low-temperature Raman spectroscopy and cathodoluminescence were used to aid the study of the origin of the SPS PL in 3C nanocrystals, indicating that the PL was not due to surface defects. A distinctive ZPL was observed at 648 nm at 80 K from ensemble measurements. A CW laser pump at 532 nm was used to excite the samples, while a pulsed 532 nm laser was used to measure the fluorescence lifetime, which results in the range of $(2 \div 5.3) \pm 0.2$ ns, depending on the treatment. Some nanocrystals provided SPSs with partial polarisation in absorption and emission. We tentatively attributed the defect responsible for SPS in 3C to the carbon antisite-vacancy pair by comparing to ensemble low-temperature PL in bulk 3C heavily irradiated sample. This defect has C_{3v} symmetry in 3C-SiC lattice (see Figure 7**a**). Because of the relatively small bandgap of 3C-SiC, the double-positive charge state was considered as possible candidates for the PL. The calculated $(2+ \mapsto +)$ charge transition level is at 1.95 eV which is very close to the ZPL energy of the bulk material defect ZPL.

SPS has also been observed in SiC nanotetrapods[19]. The tetrapod crystal phase structure consists of 3C core and 4H arms. The coexistence of 3C and 4H polytypes in these nanostructures led first to the observation of PL in the spectral region between 650 and 780 nm, not observed before in SiC nanostructures. This has been understood as a new quantum confined system accessible at room temperature. In this case, the quantum confinement and the nonclassical emission originated from the homogeneous heterostructure of 3C core and 4H legs, forming a quantum well in SiC nanotetrapod. The schematic of the SiC tetrapods
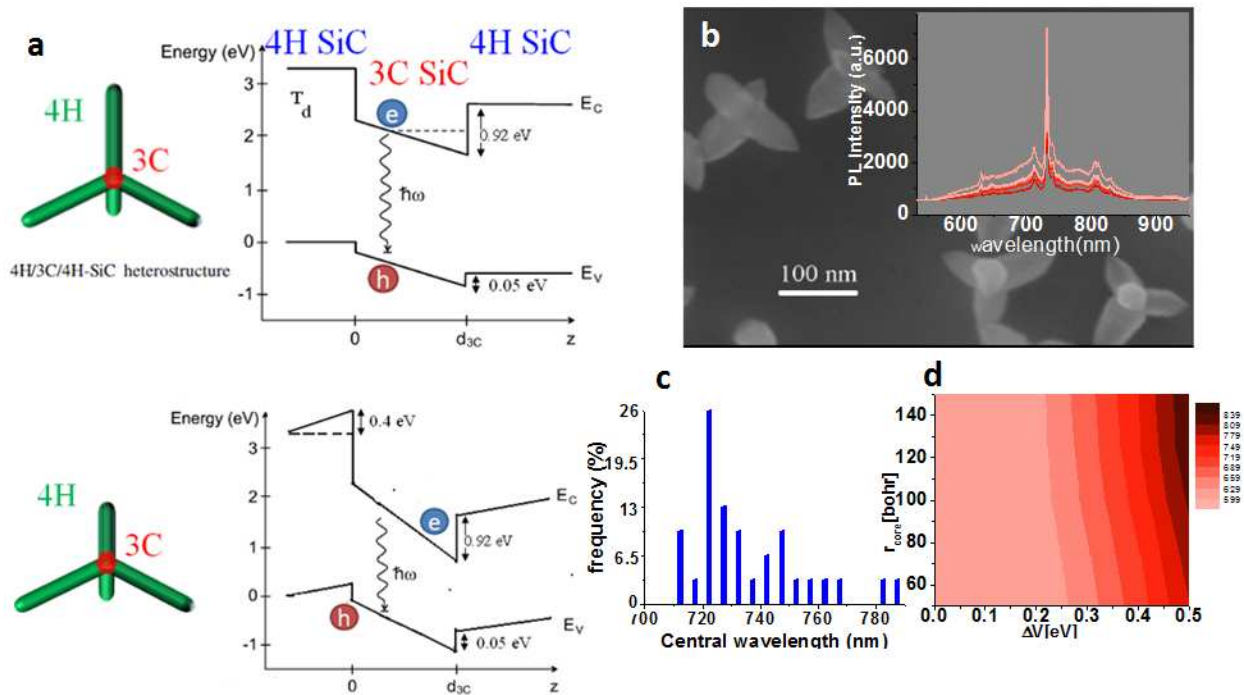
Figure 8. **a** Schematics of the tetrapod structure where the diameter of 3C core is d_{3C}. Top: Band line-up for 4H/3C/4H-SiC heterostructures for the ideal symmetry case T_d. Bottom: Quantum confinement model of SiC tetrapods when an asymmetric structure is considered and a polarisation potential change on both legs is ΔV=0.4 eV. **b** Scanning electron microscope of grown tetrapods. Every tetrapod has an average leg length of $\sim$ 100 nm. Inset: exemplary PL form a single tetrapod corresponding to an SPS.**c** Measured ZPL central emission for SPS in single nanotetrapods. **d** Calculated emission wavelengths from this model where ΔV is the potential difference along the arms and r_{core} is the radius of the 3C core, respectively. The steep potential curve with a height of ΔV arises from the different lengths of the 4H-SiC legs of a tetrapod[19]

is shown in Figure 8, accompanied by a high-resolution scanning electron microscope (SEM) image of the tetrapods. The nanotetrapods were measured to have an average leg length of 100 nm and leg diameter smaller than 50 nm, while the core was estimated as small as several nanometres. The possible band structure in SiC tetrapods is analysed by means of quantum mechanical simulations on a simplified model. The exciton is confined along the quasi one-dimensional potential curve created by 4H(leg)- 3C(core)- 4H(leg) structure. The emission wavelength of the individual tetrapods depends on their geometry, particularly, on their global symmetry, and much less on the diameter of 3C core (Figure 8 **c**). If the length of 4H legs was the same for all tetrapods (global T_d symmetry), then a classical rectangular quantum well forms for the electrons in the conduction band (0.92 eV) and a minor potential barrier for the holes in the valence band (0.05 eV), so that the potential curve does not show any steepness ($\Delta V = 0$) (Figure 8 **a** (top)). The symmetric tetrapods should show no polarisation of light. However, if the length of the 4H legs was different (i.e. not all the legs have the same length) in a SiC tetrapod, then this induces different polarisations of surface charges at the end of 4H legs in these tetrapods, so a steep potential curve ($\Delta V > 0$) both for the electrons and holes in the conduction and valence band edges (Figure 8 **a**(bottom)). This effect creates a triangular potential well for the electron in the conduction band and starts to push the hole away from 3C region.
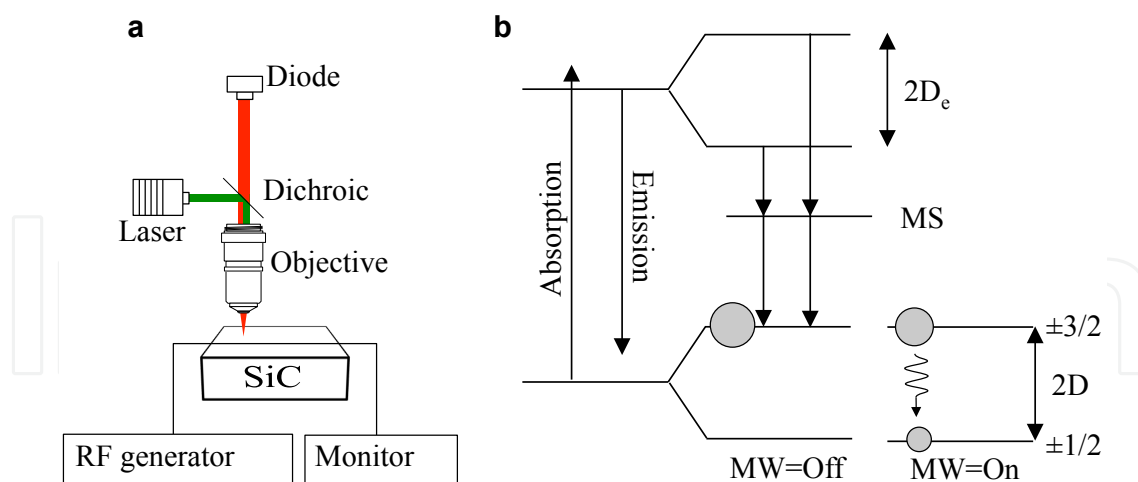
Figure 9. a Schematic of the optical set-up used to measure the ODMR signal. **b** Energy-level diagram of a spin system with a quartet ground state based on the V_{Si} [16, 37]. D and D_e denote the zero-field splitting of the ground singlet state and the excited state, respectively. The population of the spin substate levels is indicated by the grey circles. Further details in the text

5. Optical control of spin state

Spin-dependent luminescence can be used to study magnetic and hyperfine parameters for excited states of defects in SiC. A wealth of knowledge about the atomic origin of defects and their properties has been extracted from such optical measurements. More recently, with the emergence of quantum information processing technologies, optical methods have been developed to coherently control and read out the spin of a defect centre. Figure 9**a** shows a schematic of a basic set-up often used to measure spin-dependent luminescence in SiC by the optically detected magnetic resonance (ODMR) technique. The main components are the excitation laser, a dichroic mirror and a diode to collect the filtered light in the spectral region of interest. A microwave carrying wire lays in close proximity to the probed defects, and an external magnetic field may also be applied. The electron paramagnetic resonance (EPR) spectrum is recorded by monitoring the PL intensity, while the frequency of the applied microwave excitation is varied. Figure 9 **b** shows an example of an energy-level scheme for a defect (based on the V_{Si} [16, 37]). Firstly, the defect is optically excited. In this system, intersystem crossing (MS) causes the higher-lying spin sublevel of the ground state ($m_s = \pm 3/2$) to be preferentially populated. When resonance with an allowed EPR transition occurs on the application of a microwave field, such as $|m_s = \pm 3/2\rangle \rightarrow |m_s = \pm 1/2\rangle$, the steady-state population of the sublevels is redistributed. This leads to an enhanced singlet ground-state absorption and an increase in the PL intensity. Decreases in PL can also be observed depending on the relative values of the populating and decay rates. ODMR has only been observed for a limited number of systems, most notably for single NV centres in diamond [58] and more recently single V_{Si} [16] and $V_{Si}V_C$ [15] centres in SiC which will be discussed further below. Optically induced alignment (polarisation) of the ground-state spin sublevels of the V_{Si} in 4H- and 6H-SiC was observed recently for the first time at room temperature [59, 60]. The alignment schemes vary depending on the crystal polytype and crystallographic position of V_{Si} in the crystal lattice, as well as their zero-field splitting parameters. For 6H-SiC, the zero-field splitting parameter of V_{Si} is 9×10^{-4} cm^{-1} (26.9 MHz for the k-site) and 42.8×10^{-4} cm^{-1} (128.3 MHz for the h-site), while for 4H, it was found

to be 22×10^{-4} cm^{-1} (65.9 MHz for the h-site). The spin states of the UD-2 lines have recently been optically addressed and coherently controlled [38, 39]. In this work, with the four UD-2 lines labelled as PL1-PL4, the spin-1 ground state of each line was investigated as well as a pair of defect spin states of unidentified origin (PL5 and PL6). Room temperature Hahn echo measurements of these latter two defects was demonstrated with T_2^* times of 214 ns and 1248 ns, respectively, similar to the V_{Si} defect. The spin coherence times were found to be comparable to those of the NV in diamond[61]. Such measurements have been performed in 3C, 4H and 6H polytypes with defects existing in the as-grown material or those formed by ion implantation [39]. The UD-2 family of PL lines in 6H-SiC also show ODMR signals and are labelled QL1-QL6. The QL1 line is associated with a spin system with a zero-field splitting of 1.299 GHz. In contrast to conventional EPR where the transverse magnetisation of a large spin ensemble is detected, ODMR can have single spin sensitivity due to linking weakly allowed magnetic dipole transitions to highly allowed electric dipole emission processes. Optically addressing and coherently controlling the spin state of single defect is a potential basis for quantum information and nanoscale sensing applications. This has recently been demonstrated [15, 16] by using a range of pulsed ODMR techniques. Many of the detection and pulse sequences developed for EPR can be applied to ODMR experiments with minor modifications. Such measurements have allowed unprecedented insight into the spin of defects at the ensemble concentration level and now to the single-defect level. Figure 10 shows two ODMR modes of operation as applied to a single V_{Si} defect in SiC [16]. For this centre, spin transitions between ground state sublevels are induced by the microwave excitation giving rise to an enhancement of the PL intensity (Figure 10a and b). The line width is 6 MHz and is limited by the inhomogeneous spin coherence time T_2^* with laser and microwave power broadening effects superimposed. Pulsed methods can be used to circumvent this. Figure 10c shows a simple sequence of pulses that can be used to measure the Rabi oscillations, the characteristic signature of a coherent system interacting with an electromagnetic field. Oscillations reflect the behaviour of a population of an excited state as a function of the input pulse area or qubit rotations. The microwave frequency is set to resonance and the oscillation period is proportional to the microwave field strength. The largest Rabi frequency measured was 8.4 MHz ($B_1 = 0.16$ mT), corresponding to a $\pi/2$ rotation in about 30 ns. Interactions of the spin system with its environment cause a relaxation of polarisation and coherence and are characterised by two time constants, the longitudinal time T_1 (spin-lattice relaxation time) and the transverse relaxation time T_2 (spin-spin relaxation time). Long spin coherence is essential for quantum information and sensing applications. Using a Hahn-echo pulse sequence ($\pi/2 - \tau - \pi - \tau' -$projection), Widmann $et\ al.$ placed a lower bound to the spin coherence time of 160 μs and an upper bound of 1 ms, limited by the spin relaxation time. The accuracy was limited by modulations in the signals possibly due to hyperfine coupling to a ^{29}Si nuclear spin close by. These long coherence times collected at room temperature are an indication that SiC is a promising platform for quantum technologies. The main issues are the weak PL intensities (40 kcts/s when integrated with a solid immersion lens) and the poor ODMR contrast ($< 1\%$). Christle et al.[15] report the coherent control of the electronic spin of individual neutral divacancies with emission in the NIR compatible with telecommunication wavelengths. At a temperature of 20 K, a coherence time of 1.2 ms was obtained. The inhomogeneous spin dephasing time, T_2^*, measured by a Ramsey pulse sequence, $\pi/2 - \tau - \pi/2$, was found to be up to 4.4 μs. These were longer than that observed earlier for ensembles [38]. A spin coherence time of 1.2 ms was also deduced for a spin ensemble rather than on a single-defect level owing to
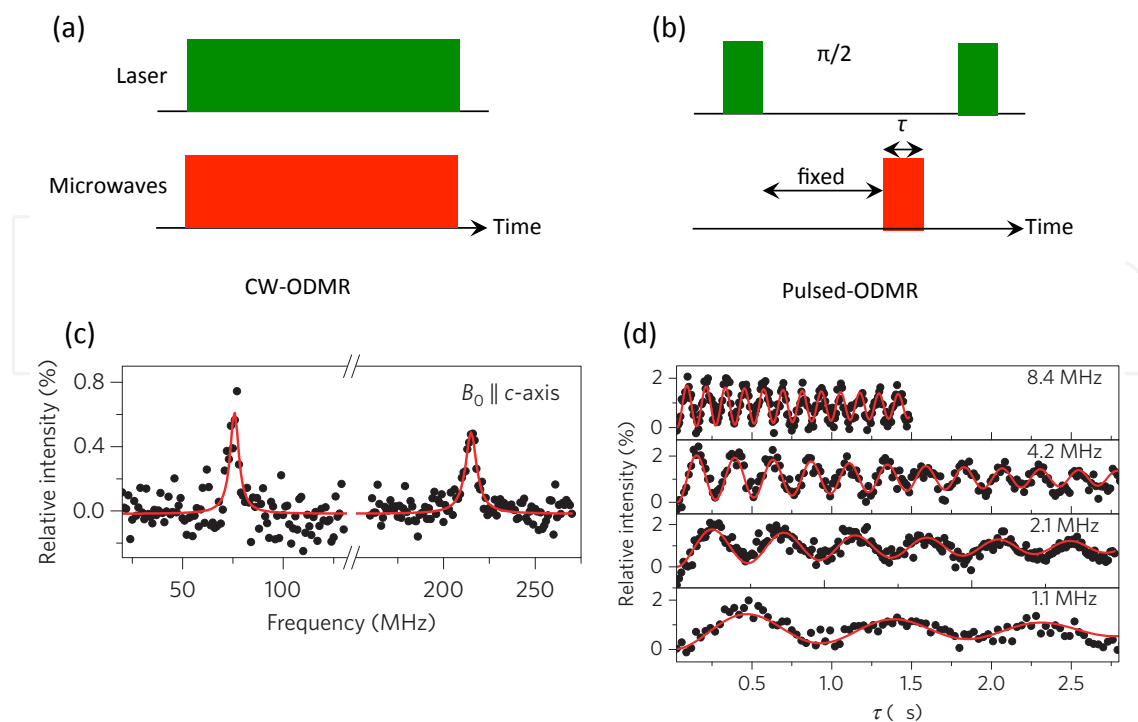
Figure 10. a Schematic of the continuous wave ODMR method with the microwave frequency varied while the PL is measured. **b** Pulse sequence used to detect spin Rabi oscillations. **b** ODMR spectrum of the V_{Si} in a magnetic field of 50 G parallel to the c-axis. **d** Spin Rabi oscillations of the $|m_s = +3/2\rangle \rightarrow |m_s = +1/2\rangle$ transition of a single V_{Si} for various field strengths B_1. **c** and **d** reprinted by permission from Macmillan Publishers Ltd: Nature Materials 14, 164, copyright (2015)[16]

limitations in their photon collection efficiency. This duration is remarkably long and much greater than that found for the NV centre in isotropically pure diamond [61]. In addition, still greater spin coherence times might be achieved if the SiC is also isotropically purified [62]. This result may be counterintuitive since the natural abundance of ^{29}Si is greater than ^{13}C. Theoretical calculations attribute this phenomenon to three factors: the longer bond length in SiC, the smaller gyromagnetic ratio of ^{29}Si and the suppression of heteronuclear spin pair flip-flop processes in the strong magnetic field regime [63]. Long-lived spin coherence is essential to implement quantum information and sensing technologies; in SiC, it seems to be a common feature of the spins in all three polytypes. Single-spin coherent control has been achieved for both the V_{Si} and $V_{Si}V_C$ centres. Although the NV centre in diamond dominates this field, SiC shows some advantages being compatible with standard device processing protocols, available in high-quality 3-inch wafers and available in a wide range of polytypes. SiC-based devices in which single spins act as the active device element may be employed in emerging quantum technologies.

6. Photonics nanocavities and micro-cavities

Spontaneous emission from an SPS can be enhanced if the defect or an equivalent 2-level system is placed inside a cavity. The magnitude of the enhancement depends on the coupling (g) between the cavity and the atom's emission modes. The enhancement of the spontaneous emission of a dipole in a cavity is the Purcell factor, given by $F =$

$3/4\pi^2 Q/V(\lambda/n)^3$, where the quality factor $Q = 2\pi\nu_c/k$ is related to the cavity resonance frequency ν_c and the cavity field decay rate k, while V is the mode volume of the cavity. Nanophotonics is recently an expanding area for quantum technologies as it can provide a strong confinement of photons in a tiny space and potential applications such as ultrasmall and integrated photonic chips, slowing and stopping lights, quantum information processing and environmental sensing. Quantum emitters in bulk materials have inherently poor directional emission, prohibiting high collection and coupling efficiencies to fibre networks for long-range communication. One approach is to utilise cavities to enhance coupling to a specific optical mode. Using a photonic-crystal waveguide yields extraordinarily high coupling efficiencies. Similarly, optical microresonators offer the possibility to increase the coupling of quantum emission with the cavity mode. SiC-based nanophotonics is recently an expanding area as it could further improve present technologies based on Si or GaAs. One reason is due to the suppression of two-photon absorption at high input powers, because of its larger bandgap. Additionally, SiC can provide broadband operation, even in the visible range. The ability to construct nanocavities and optical microdiscs in SiC will possibly allow relevant technological advance in room temperature SPSs based on SiC defects and the coupling of multi-emitters to reach strong coupling regime. The main nanofabrication advantage available in SiC is based on its routinely achievable p- and n-doped in different polytypes and in its possibility to be grown epitaxially on a sacrificial silicon substrate; these features allow dopant-selective photoelectrochemical etching[64, 65] and more amenable application of reactive ion etching procedures to nano-fabricate photonics or micro-mechanical structures[21].

6.1. SiC photonics cavities

SiC 2D-photonic nanocavity crystals were initially fabricated on thin SiC-on-insulator wafers, which were specially prepared using the smart-cut technique[66]. The main challenge for 4H and 6H is related to the fact that SiC is much harder than silicon, and therefore, the important challenges here are the preparation of SiC membrane structure and the etching of SiC material as the conventional plasma etching technique for Si cannot be used. The wafers consisted of a SiC (6H crystalline structure) surface layer with a thickness of 180 nm above an SiO_2 layer (680 nm), on top of a Si substrate (300 nm) that was used for handling. Quality factors up to 1,300 were achieved with such crystals, and their resonance tuning from the visible to the infrared can allow the selective enhancement of the SiC SPSs[12]. The PCh cavities were L3 nanocavities with three missing air holes. Designs and realisation based on schematics of air hole-shifted and heterostructured nanocavities[67] showed higher Q factors of 6×10^3 and up to 5×10^5, demonstrating that the design concepts previously used in Si can be applied to the SiC hexagonal polytypes. Regardless these were the first attempts, these PCh nanocavities showed so far the highest Q (see Figure 11). More recently 3C-SiC polytype is used for better integration with Si photonics, by heteroepitaxial growth on sacrificial Si substrate, allowing for direct patterning without ion implantation damage. With this method, an L3 PhC cavity has been fabricated in a thin-film (200 nm) 3C-SiC slab, obtaining Q-factor of 1,000 and modal volume of $0.75(\lambda/n)^3$ over the band between 1250 and 1600 nm in the telecom IR range[22]. The possibility to incorporate colour centres with optically addressable spins similar to NV centres in diamond has been shown by fabricating H1 and L3 PhC cavities in 300-nm-thick 3C-SiC, as shown in Figure 12, with experimental Q of 1,000 for the strongly coupled cavity and $(\lambda/n)^3$ mode volume, tuned to the zero phonon line of the Ky5 colour
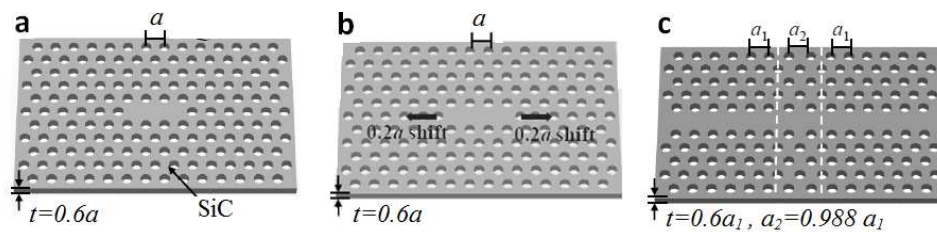
Figure 11. Schematics of **a** SiC-based (L3) nanocavity with three missing air holes and a $Q \approx 1200$; **b** air hole-shifted $Q \approx 6000$ and A**c** heterostructured PCh nanocavity with higher Q obtained in 6H polytype, $Q \approx 500000$. a is the cavity lattice constant related to the holes radius that for NIR range of $1380 \div 1590$ nm is a = 550 nm[11]. Lattice constant as small as a=150 nm was achieved for resonance frequencies at 550-600 nm. Image adapted from ref[11]

centre (emission band 1,100 to 1,300 nm at 20 K), enhancing PL collection up to 10 times[23]. PhC structures made by a square or hexagonal lattice of SiC rods in air have also been proposed for telecom band applications[28], resulting in the confinement of the cavity mode in air, with the aim of reducing modal dispersion and temperature sensitivity. Theoretical modelling of a defect A1 cavity in SiC hexagonal lattice (photonic bandgap, PBG, from 1,380 to 1,850 nm) showed a thermal shift of the cavity TE mode seven times smaller as compared to a Si-based lattice with similar PBG, for a temperature range between 25 and 200 °C, with a maximum Q of 224. The highest Q reported to date of 7.69×10^4 has been achieved using a 45-μm-long 1D PhC nanobeam cavity at 1.5 μm wavelength [29]. It was fabricated on a 280-nm-thick amorphous SiC (a-SiC) film, deposited on an Si substrate by plasma-enhanced chemical vapour deposition (PECVD) in a gas mixture of silane and methane and patterned by e-beam lithography and reactive-ion etching with CF_4/O_2 plasma. The nanobeam was released in KOH with subsequent critical point drying.

6.2. SiC microresonators

High-Q optical microresonators can also dramatically enhance optical fields inside a small volume and are considered relevant in applications to enhance nonlinear optics effects and their implication to quantum optics. In addition, they are important in fields such as cavity optomechanics[68, 69]. In general for microresonators, the materials play a crucial role based on its properties such as linear/nonlinear optical susceptibilities and mechanical property. High-Q microresonators generally exhibit large thermal and mechanical sensitivities, making them desired for practical application. Microresonators are commonly fabricated in disc shapes resting on a central pedestal; however, recently suspended ring resonators have been proposed in order to obtain better waveguide dispersion engineering properties for nonlinear processes[20]. Some materials, such as Si and GaAs, have small bandgaps that limit the operating spectral range. Others, such as lithium niobate and chalcogenide glass, exhibit photorefractive effect or two-photon absorption and strong Raman scattering, making it challenging to handle high optical powers. For microphotonic/nanophotonic applications, it is crucial to search for a material platform with combined superior optical, mechanical and thermal properties. SiC seems to match some of these requirements for an optimal microresonator performance. Since strong coupling between a point defect optical source and the resonant cavity is challenging, due to having to place the defect at the field maximum of the cavity mode, a disc resonator in this respect has the good feature of supporting multiple modes, which cover almost the whole volume of the disc, making overlapping and tuning to

the zero phonon line of the defect easier[26]. The single-crystalline 3C-SiC in Lu et al.[21] was epitaxially grown on a (100) silicon substrate by the two-step atmospheric pressure chemical vapour deposition. A disc geometry was patterned by electron-beam lithography and etched by reactive ion etching with CF_4/Ar plasma, optimised to form the well-defined device structure. The silicon substrate was undercut by XeF_2 to form the supporting pedestal. The intrinsic Q factor is shown to be 6.19×10^3. The damage to the crystal incurred during ion etching can impair the optical efficiency and the spin coherence of the defect sources, so an alternative is sought by low-damage selective chemical etch processes, such as photoelectrochemical etching, exploiting the higher etch rate of n-doped to p-doped material under direct UV illumination in HF or KOH solutions[24]. Epitaxial p-doped SiC on n^+-SiC was patterned by reactive-ion etching (RIE) in SF_6/O_2 plasma using 3 μm alumina microspheres as masking agents; then the p-layer was undercut by KOH etching under UV illumination. Well-undercut microdiscs reached a measured Q-factor of 9,200 at 617.4 nm resonance, with a theoretical maximum of 10^5, limited by light leakage into the supporting pillar. The issue of light loss in the supporting Si substrate was addressed by exploiting the high stiffness of an 860-nm-thick 3C-SiC layer, building a 20 μm radius ring microresonator suspended in air from a central pedestal by 200-nm-wide spokes and by e-beam lithography followed by CHF_3/O_2 RIE[20]. An intrinsic Q factor of 14,100 was measured at 1,543 nm wavelength. PL from 3C-SiC in the visible range was first demonstrated for multi-emitter cavity quantum electrodynamics at room temperature in disc microresonators of 210 nm thickness and diameter below 2 μm, fabricated by two-step chemical vapour deposition (CVD) followed by e-beam patterning, HBr/Cl_2 plasma etching and XeF_2 undercut to form the pedestal[30]. Characterisation by laser scanning confocal microscopy between 650 and 850 nm wavelength evidenced whispering gallery modes with Q-factor up to 2,300 and mode volume around $2 \times (\lambda/n)^3$. The highest Q-factor reported to date for a disc microresonator is 5.12×10^4, obtained at 1,551 nm wavelength with e-beam-patterned heteroepitaxial 3C-SiC on Si, ion etched in CF_4/Ar plasma with subsequent KOH undercut[26]. The resulting disc had a thickness of 700 nm and a radius of 6.25 μm, and simulations showed a strong coupling regime with a cooperativity C=20 and a maximum theoretical radiation-limited Q-factor above 10^8.

6.3. Nonlinear effects

SiC is a non-centrosymmetric material, which means that it has nonzero second-order susceptibility, permitting the observation of nonlinear effects such as second-harmonic generation (SHG), and Pockels effect, which are not available in the more common centrosymmetric materials (SiO_2, SiN_x and others whose molecule's symmetry allows only third-order susceptibility). Differently from other non-centrosymmetric semiconductors and crystals such as $LiNbO_3$, SiC has the ability to house optically active defects for quantum processing. Nonlinear effects in this material combined with colour centres have the potential to increase the applications in other fields such as nonlinear photonic, including all-optical switching, wavelength conversion and harmonic generation. These effects are important for the development of quantum devices based on nonlinear effects[70]. SiC second order, $\chi^{(2)}_{i,j,k}$, and electro-optical $r_{i,j,k}$ coefficients were predicted from ab initio calculations in 3C, 4H and 6H [71] and measured [72–75] in 4H and 6H polytypes. Second-order nonlinear optical coefficients are at the core of the physics of nonlinear optical processes; their knowledge and high values are essential to increase the efficiency of frequency conversion. Hexagonal SiC is
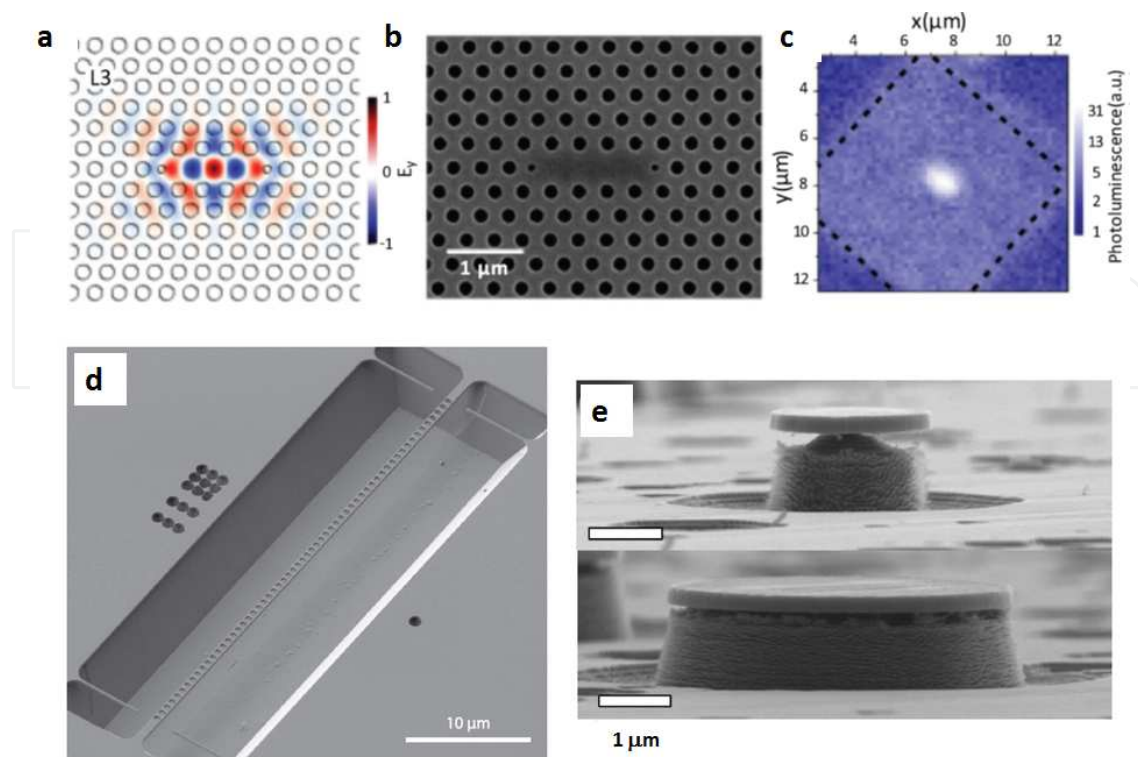
Figure 12. a Simulated E_y field distribution, **b** SEM image and **c** PL at 20K from an L3 photonic-crystal cavity in 3C-SiC. The cavity resonance is tuned by size reduction and shift of the neighbouring crystal holes, for 1,060 nm excitation of the embedded Ky5 colour centre[23]. **d** SEM image of a fabricated a-SiC 45-μm-long PhC nanobeam cavity, achieving the highest Purcell factor reported of 10^4 at 1.5 μm wavelength[29]. **e** SEM micrographs of high-Q disc resonators obtained by low-damage photoelectrochemical selective etching of p-SiC over n$^+$-SiC. Notice the different undercuts achieved by wet etching and the surface porosity of the supporting pillar, which does not affect the etched microdisc[24]. Images reproduced from [23, 24, 29] with Copyright permission 2014-2015, AIP Publishing LLC

characterised by three independent components of the second-order nonlinear optical tensor, recently measured accurately as $d_{31} = d_{32} = 6.7(6.5)\text{pm/V}$, $d_{15} = d_{24} = 6.5(6.7)\text{pm/V}$ and $d_{33} = -12.5(-11.7)\text{pm/V}$ in 6H (4H). The refractive indices and the birefringence are used to determine if phase matching can be realised; they have been remeasured from the visible to the mid-infrared region, and Sellmeier equations for ordinary and extraordinary refractive index in 4H and 6H have been provided[76]. This has led to mid-infrared region laser output tunable from 3.90 to 5.60 μm by phase-matched difference frequency generation in 4H-SiC. In this case, the material can withstand high power and for laser higher outputs in this spectral region. For applications, it is important to enhance SHG in photonics cavities. The first demonstration of SHG in SiC-based nanophotonic structures used a 6H-SiC PhC cavity tuned to 1560 nm with a Q of 10,000, taking advantage of the high refractive index of SiC (2.5) to increase confinement and of the large electronic bandgap (3.0 eV) to extend the operating bandwidth from IR to visible and to suppress two-photon absorption. A conversion efficiency of 2.59×10^{-5} was obtained for 0.17 mW average input power[25]. A high-Q amorphous SiC disc microresonator has been demonstrated for nonlinear applications, with an optical Q of 1.3×10^5 in the 1,550 nm telecom band[27]. With PECVD deposition followed by e-beam patterning and plasma etching, a smooth-sidewall disc with 570 nm thickness and 6 μm radius was fabricated, and its Kerr nonlinearity was characterised with a pump-probe self-/cross-phase modulation scheme using two high-Q

whispering-gallery modes. The resonator was pumped at 1545 nm with sinusoidally modulated light, transferring the modulation on the refractive index due to optical Kerr effect, which was then measured by a weak probe signal coupled at 1,498 nm. This gave a nonlinear coefficient $n_2 = 5.9 \times 10^{-15}$ cm^2/W, higher than any other material in use to generate frequency combs. Recently, SHG microscopy was used as a non-invasive method for imaging and identification of structural defects such as polytype inclusions and stacking faults in SiC epilayers, grown on hexagonal SiC by the vapour-liquid-solid techniques. This technique is competitive with destructive sample preparation and severely limited area of analysis to tens of microns associated instead with high-resolution TEM. By combining the SHG-based imaging with X-ray diffraction and SHG rotational anisotropy, the growth of 3C polytype on the 4H-SiC substrate was confirmed, and the polytype of the imaged defects was identified[77].

7. Other applications

Paramagnetic defects in SiC have been integrated into some devices as a proof of principle demonstration of their electrical control or of their ability to sense changes in strain, magnetic field and temperature. The discovery of single-photon emission and its engineering and isolating single defects with proper transition energy on demand can open a route for an efficient electrical single-photon source, particularly in the IR region, due to the described subgap defects. To fabricate devices, standard semiconductor manufacturing technology in combination with high-energy electron irradiation of the material can allow, for instance, the construction of LEDs with radiative recombination occurring at irradiation-induced intrinsic defects. Such LEDs have been demonstrated with two strong PL emission bands in the visible and near infrared (NIR), associated with two different intrinsic defects, one being the Si vacancy[78]. Selective manipulation of individual defect spin can be achieved. The spin separation required to achieve strong dipolar coupling between spins is of the order of tens of nanometres. Electric fields can be confined on similar length scales; therefore, electrically driven spin resonance methods can be used to manipulate the defect spin state[79]. Divacancy defects in 4H- and 6H-SiC possess a spin-dependent optical cycle, which allows non-resonant laser illumination to polarise first and then read out its ground-state spin. Since the defect PL depends on whether its spin state is $m_s = 0$ or $m_s = \pm 1$, it is possible to control the defect spin dynamics by the measuring differential PL (ΔI_{PL}) between an initial state and one that has been evolved by applying a magnetic or electric field pulses. These ΔI_{PL} measurements, in addition to enabling conventional (magnetically driven) ODMR, can also be used for electrically driven ODMR (EODMR). In Figure 13, we show the electrical control of the QL1 (unknown yet) defect in 6H-SiC with similar spin properties of the neutral divacancies, with ZPL at 1.088 eV and ODMR at 1.3GHz[39]. Ac electric fields are used to drive the Rabi oscillations across a magnetic-dipole forbidden spin transition ($m_s = \pm 2$) of the optically addressable electronic spin. A flow cryostat cools the device illustrated in Figure 13**b** to 20 K, and a permanent magnet is used to provide a static magnetic field parallel to the defect magnetic dipole. QL1 colour centres were produced in 6H-SiC substrates via a carbon implantation and annealing process introducing defects immediately below the surface. The spins were localised within a 400-nm-thick layer immediately beneath the 6H-SiC surface and were optically pumped with a 976 nm laser addressing 10^4 defects in the optical excitation volume. We show in Figures 13 **c** and **d** the effect observed from the application of an electric field via the electrode to the transition corresponding to the
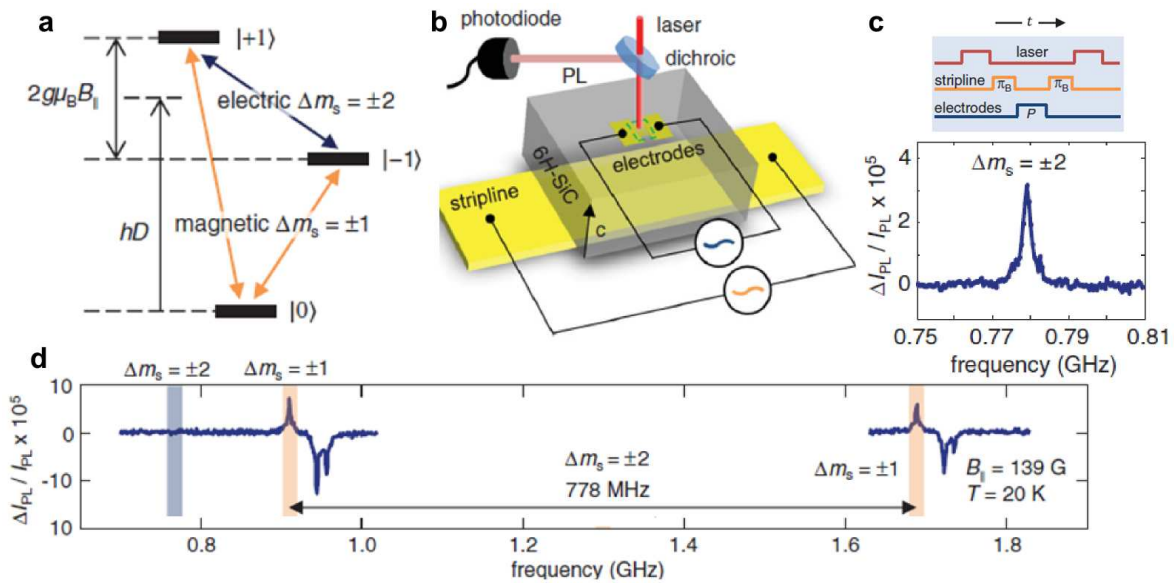
Figure 13. a The ground state spin structure of QL1 defect in 6H-SiC, where the spin levels $m_s = 0, \pm1$ are shown in the presence of a magnetic field $B_\parallel$. The allowed optical transition $m_s = \pm1$ are in orange, while the $m_s = \pm2$ in blue are not allowed. **b** Experimental set-up used for PL collection via a dichroic mirror and measured with a photodiode. The spins are driven electrically by the electrodes and magnetically by the stripline directly on the bulk material.**c** A clear EODMR feature is observed at the frequency difference (778 MHz) of the $m_s = |+1\rangle$ and $m_s = |-1\rangle$, indicating population transfer across the two levels. On the top of the panel, the time sequence of the microwave pulse and the electric field are applied to achieve EODMR. The length of P is fixed and its frequency is swept. The electrode power was 0.09 W and the magnetic $B_\parallel$=139 G.**d** ODMR signal when the stripline is driven at $B_\parallel$=139 G. The $m_s = \pm1$ resonances are shaded orange, and the $m_s = \pm2$ resonance (at 778 MHz, shaded blue) is not seen in ODMR only. Images reproduced from [79] with Copyright permission 2014 American Physical Society

prohibited optical transition. Another PL resonance appears in the presence of the $m_s = \pm2$ transition indicating a population transfer between the two-spin states.

Falk et al.[80] state that the spin states of neutral divacancies in 4H-SiC are highly sensitive to electrical and mechanical perturbations of material. The experiments were done in high-purity semi-insulating 4H-SiC wafers, purchased from Cree Inc., where neutral divacancies were incorporated during crystal growth. A 50 μm membrane from the sample was cut and mounted on top of a piezo actuator. The piezo actuation applies tensile strain to the SiC membrane perpendicular to the c-axis. The device was cooled to 20 K. The neutral divacancy's ZPLs were excited optically at 976 nm and monitored. Microwave excitation for electron spin resonance was supplied by waveguide antennae on the chip. A variation of the ODMR signal was observed in the presence of strain. The strain sensitivity is inferred to be $10^{-7}/\sqrt{HzN}$, where N is the number of spins. Also, the electric field response exhibited significant spin-dependent PL, 2-7 times stronger than with NV centres in diamond. Electric field pulses were applied across the SiC membrane, using patterned electrodes that transmit light, and the ODMR signal was monitored. If these techniques were extended to single defects, these properties could be applicable to the nanometre scale, and they could be applied for sensing intracellular electric fields, integrating nanoscale sensing into SiC bioelectronics[81], or coupling spins to SiC nano-mechanical resonators[9]. In another work, the spin resonances of the V_{Si} defect at 128 MHz and 28 MHz associated with the V2 and V3 ZPLs in 6H SiC were used to monitor magnetic field and temperature variation [82].

An important milestone is to achieve the integration of these defects in nanoparticles. The first demonstration of optical spin control of silicon vacancy in 600-nm-size material was achieved in [83]. High-quality, defect-free 6H-SiC bulk material using the well-established sublimation technique in argon atmosphere at a high temperature ($2500 \div 2600\,^{\circ}$C) was grown from a specially prepared source pure SiC powder synthesised from silicon and carbon mixture of spectral purity. Macroscopic crystal fragments in the mm range were synthesised and then placed in the central irradiation tube of a TRIGA Mark II nuclear reactor, where vacancies were formed by neutron irradiation followed by annealing, achieving an initial concentration of V_{Si} defects of the order of 10^{15} cm^{-3}. High-energy milling process was used to achieve size from 60 to 600 nm. PL from V_{Si} ($V_{1,2,3}$) was observed in 60 nm and 600 nm crystals at room and cryogenic temperature for comparison to identify the ZPLs. No single-photon emission was observed while V_3 and V_2 from V_{Si} spin resonances were observed at 27 MHz and 127 MHz with positive and negative ODMR contrast, respectively.

8. Summary and outlook

We have summarised SiC paramagnetic defects with quantum properties observed following single-defect creation and isolation. These defects are present in various polytypes, and their variety in different crystal sites increases their space of applications. We also reviewed the state of the art of quantum effects observed in SiC nanostructures. SiC as a host for quantum systems is just at its inception, though the beginning indicates it could be one of the most prominent and rich material to investigate or to employ in the future. A large variety of deep defects were investigated from the point of view of paramagnetic and optical properties in the past, and now other quantum properties have been revealed, providing additional information not available at the ensemble level and novel insights relative to previously known defects. The challenge of engineering a desired defect in a specific location in the material is still an open problem, though it has been successfully demonstrated so far with electron, neutron and ion irradiation. SiC single defects in bulk and in the red part of the spectrum is one of the best SPS operating at room temperature, surpassing in terms of brightness other materials. The properties of these defects are also important for their spin coherent control and their use as spin qubits. The spin coherence time in ensemble and at the single level of intrinsic defects in SiC is very promising and comparable to NV in diamond. Isolation of intrinsic single spin has been achieved. However, for the most interesting spectral region in the infrared, it appears that the emission is not very bright and needs further enhancement via integration of the defects in photonics crystal cavities or microresonator. The spin coherence control still requires cryogenic temperature for the IR emitters. Since both Si and C have spin-free isotopes (^{28}Si^{12}C), it is expected that the measured coherence times could be enhanced through the sublimation crystal growth to reduce the abundance of ^{29}Si and ^{13}C isotopes having nonzero nuclear spins. While the challenge of the nano-fabrication of this material seems to indicate its feasibility and viability, for this to be successful, a major challenge needs to be addressed, specifically, the creation of the defects in a specific location close to the material surface within the photonic devices. Another option could be to integrate SiC QDs in hybrid photonics systems. This will require the successful incorporation of the desired defects with high yield in QDs and NPs. Additionally, many other potential defects in the material should be explored, particularly extrinsic defects that could facilitate their on-demand integration in devices. Alternatively for intrinsic defects originated from damage, more precise damage techniques could aid to the accurate location of the defects in

the lattice. Nanostructures are ready to be integrated with deep optical and paramagnetic defects, though better design of cavities and choice of higher quality material would allow to take full advantage of functionalities related to single-photon emission and spin sensing to further advance their current applications. If all these challenges will be overcome in the next years, we envision the construction of SiC-defect-based LEDs and photonic crystal structures with in-built active quantum systems, for next-generation quantum technology devices.

Author details

Stefania Castelletto[1*], Lorenzo Rosa[2,3] and Brett C. Johnson[4]

*Address all correspondence to: stefania.castelletto@rmit.edu.au

1 School of Aerospace, Mechanical and Manufacturing Engineering RMIT University, Melbourne, Australia

2 Swinburne University of Technology, Centre for Micro-Photonics (H74), Hawthorn, Australia

3 University of Parma, Department of Information Engineering, Parma, Italy

4 School of Physics, The University of Melbourne, Parkville, Australia

References

[1] C. A. Zorman, A. J. Fleischman, A. S. Dewa, M. Mehregany, C. Jacob, S. Nishino, and P. Pirouz, "Epitaxial growth of 3C-SiC films on 4 in. diam (100) silicon wafers by atmospheric pressure chemical vapor deposition," J. Appl. Phys. **78**, 5136–5138 (1995).

[2] R. Madar, "Materials science: Silicon carbide in contention," Nature **430**, 974–975 (2004).

[3] A. Dzurak, "Quantum computing: Diamond and silicon converge," Nature **479**, 47–48 (2011).

[4] D. DiVincenzo, "Quantum bits: Better than excellent," Nat. Mater. **9**, 468–469 (2010).

[5] J. R. Petta, A. C. Johnson, J. M. Taylor, E. A. Laird, A. Yacoby, M. D. Lukin, C. M. Marcus, M. P. Hanson, and A. C. Gossard, "Coherent manipulation of coupled electron spins in semiconductor quantum dots," Science **309**, 2180–2184 (2005).

[6] M. Hofheinz, H. Wang, M. Ansmann, R. C. Bialczak, E. Lucero, M. Neeley, A. D. O'Connell, D. Sank, J. Wenner, J. M. Martinis, and A. N. Cleland, "Synthesizing arbitrary quantum states in a superconducting resonator," Nature **459**, 546–549 (2009).

[7] J. J. Pla, K. Y. Tan, J. P. Dehollain, W. H. Lim, J. J. L. Morton, D. N. Jamieson, A. S. Dzurak, and A. Morello, "A single-atom electron spin qubit in silicon," Nature **489**, 541–545 (2012).

[8] G. Davies and M. F. Hamer, "Optical studies of the 1.945 ev vibronic band in diamond," Proc. R. Soc. Lond., Ser. A **348**, 285–298 (1976).

[9] Y. T. Yang, K. L. Ekinci, X. M. H. Huang, L. M. Schiavone, M. L. Roukes, C. A. Zorman, and M. Mehregany, "Monocrystalline silicon carbide nanoelectromechanical systems," Appl. Phys. Lett. **78**, 162–164 (2001).

[10] C. A. Zorman and R. J. Parro, "Micro- and nanomechanical structures for silicon carbide mems and nems," Physica Status Solidi B **245**, 1404–1424 (2008).

[11] B.-S. Song, S. Yamada, T. Asano, and S. Noda, "Demonstration of two-dimensional photonic crystals based on silicon carbide," Opt. Express **19**, 11084–11089 (2011).

[12] S. Yamada, B.-S. Song, T. Asano, and S. Noda, "Silicon carbide-based photonic crystal nanocavities for ultra-broadband operation from infrared to visible wavelengths," Appl. Phys. Lett. **99**, 201102 (2011).

[13] S. Castelletto, B. C. Johnson, and A. Boretti, "Quantum effects in silicon carbide hold promise for novel integrated devices and sensors," Adv. Opt. Mater. **1**, 609–625 (2013).

[14] S. Castelletto, B. Johnson, V. Ivády, N. Stavrias, T. Umeda, A. Gali, and T. Ohshima, "A silicon carbide room-temperature single-photon source," Nat. Mater. **13**, 151–156 (2014).

[15] D. J. Christle, A. L. Falk, P. Andrich, P. V. Klimov, J. U. Hassan, N. T. Son, E. Janzén, T. Ohshima, and D. D. Awschalom, "Isolated electron spins in silicon carbide with millisecond coherence times," Nat. Mater. **14**, 160–163 (2015).

[16] M. Widmann, S.-Y. Lee, T. Rendler, N. T. Son, H. Fedder, S. Paik, L.-P. Yang, N. Zhao, S. Yang, I. Booker, A. Denisenko, M. Jamali, S. A. Momenzadeh, I. Gerhardt, T. Ohshima, A. Gali, E. Janzén, and J. Wrachtrup, "Coherent control of single spins in silicon carbide at room temperature," Nat. Mater. **14**, 164–168 (2015).

[17] F. Fuchs, B. Stender, M. Trupke, J. Pflaum, V. Dyakonov, and G. V. Astakhov, "Engineering near infrared single photon emitters in ultrapure silicon carbide," Nat. Comm. (2015). doi:10.1038/ncommos8578 .

[18] S. Castelletto, B. C. Johnson, C. Zachreson, D. Beke, I. Balogh, T. Ohshima, I. Aharonovich, and A. Gali, "Room temperature quantum emission from cubic silicon carbide nanoparticles," ACS Nano **8**, 7938–7947 (2014).

[19] S. Castelletto, Z. Bodrog, A. P. Magyar, A. Gentle, A. Gali, and I. Aharonovich, "Quantum-confined single photon emission at room temperature from SiC tetrapods," Nanoscale **6**, 10027–10032 (2014).

[20] J. Cardenas, M. Zhang, C. T. Phare, S. Y. Shah, C. B. Poitras, B. Guha, and M. Lipson, "High Q SiC microresonators," Opt. Express **21**, 16882–16887 (2013).

[21] X. Lu, J. Y. Lee, P. X.-L. Feng, and Q. Lin, "Silicon carbide microdisk resonator," Opt. Lett. **38**, 1304–1306 (2013).

[22] M. Radulaski, T. M. Babinec, S. Buckley, A. Rundquist, J. Provine, K. Alassaad, G. Ferro, and J. Vučković, "Photonic crystal cavities in cubic (3c) polytype silicon carbide films," Opt. Express **21**, 32623–32629 (2013).

[23] G. Calusine, A. Politi, and D. D. Awschalom, "Silicon carbide photonic crystal cavities with integrated color centers," Appl. Phys. Lett. **105**, 011123 (2014).

[24] A. P. Magyar, D. Bracher, J. C. Lee, I. Aharonovich, and E. L. Hu, "High quality sic microdisk resonators fabricated from monolithic epilayer wafers," Appl. Phys. Lett. **104**, 051109 (2014).

[25] S. Yamada, B.-S. Song, S. Jeon, J. Upham, Y. Tanaka, T. Asano, and S. Noda, "Second-harmonic generation in a silicon-carbide-based photonic crystal nanocavity," Opt. Lett. **39**, 1768–1771 (2014).

[26] X. Lu, J. Y. Lee, P. X.-L. Feng, and Q. Lin, "High q silicon carbide microdisk resonator," Appl. Phys. Lett. **104**, 181103 (2014).

[27] X. Lu, J. Y. Lee, S. Rogers, and Q. Lin, "Optical kerr nonlinearity in a high-q silicon carbide microresonator," Opt. Express **22**, 30826–30832 (2014).

[28] J. Boruah, Y. Kalra, and R. Sinha, "Demonstration of temperature resilient properties of 2D silicon carbide photonic crystal structures and cavity modes," Optik - Int. J. Light Electron Opt. **125**, 1663–1666 (2014).

[29] J. Y. Lee, X. Lu, and Q. Lin, "High-Q silicon carbide photonic-crystal cavities," Appl. Phys. Lett. **106**, 041106 (2015).

[30] M. Radulaski, T. M. Babinec, K. Müller, K. G. Lagoudakis, J. L. Zhang, S. Buckley, Y. A. Kelaita, K. Alassaad, G. Ferro, and J. Vučković, "Visible photoluminescence from cubic (3c) silicon carbide microdisks coupled to high quality whispering gallery modes," ACS Photonics **2**, 14–19 (2015).

[31] E. Sörman, N. T. Son, W. M. Chen, O. Kordina, C. Hallin, and E. Janzén, "Silicon vacancy related defect in 4h and 6h sic," Phys. Rev. B **61**, 2613–2620 (2000).

[32] N. Mizuochi, S. Yamasaki, H. Takizawa, N. Morishita, T. Ohshima, H. Itoh, and J. Isoya, "Continuous-wave and pulsed epr study of the negatively charged silicon vacancy with $s = \frac{3}{2}$ and C_{3v} symmetry in n-type $4h - \mathrm{SiC}$," Phys. Rev. B **66**, 235202 (2002).

[33] J. Steeds, G. Evans, L. Danks, S. Furkert, W. Voegeli, M. Ismail, and F. Carosella, "Transmission electron microscope radiation damage of 4h and 6h sic studied by photoluminescence spectroscopy," Diam. Relat. Mater. **11**, 1923–1945 (2002).

[34] N. T. Son, P. Carlsson, J. ul Hassan, E. Janzén, T. Umeda, J. Isoya, A. Gali, M. Bockstedte, N. Morishita, T. Ohshima, and H. Itoh, "Divacancy in 4H-SiC," Phys. Rev. Lett. **96**, 055501 (2006).

[35] T. Umeda, N. T. Son, J. Isoya, E. Janzén, T. Ohshima, N. Morishita, H. Itoh, A. Gali, and M. Bockstedte, "Identification of the carbon antisite-vacancy pair in 4*h*-sic," Phys. Rev. Lett. **96**, 145501 (2006).

[36] J. W. Steeds, "Photoluminescence study of the carbon antisite-vacancy pair in 4h- and 6h-sic," Phys. Rev. B **80**, 245202 (2009).

[37] H. Kraus, V. Soltamov, D. Riedel, S. Väth, F. Fuchs, A. Sperlich, P. Baranov, V. Dyakonov, and G. Astakhov, "Room-temperature quantum microwave emitters based on spin defects in silicon carbide," Nat. Phys. **10**, 157–162 (2014).

[38] W. F. Koehl, B. B. Buckley, F. J. Heremans, G. Calusine, and D. D. Awschalow, "Room temperature coherent control of defect spin qubits in silicon carbide," Nature **479**, 84 (2011).

[39] A. L. Falk, B. B. Buckley, G. Calusine, W. F. Koehl, V. V. Dobrovitski, A. Politi, C. A. Zorman, P. X.-L. Feng, and D. D. Awschalom, "Polytype control of spin qubits in silicon carbide," Nat. Commun. **4**, 1819 (2013).

[40] B. Magnusson and E. Janzén, "Optical characterization of deep level defects in SiC," Mater. Sci. Forum **340342**, 341–346 (2005).

[41] N. T. Son, P. N. Hai, M. Wagner, W. M. Chen, A. Ellison, C. Hallin, B. Monemar, and E. Janzén, "Optically detected magnetic resonance studies of intrinsic defects in 6H-SiC," Semicond. Sci. Technol. **14**, 1141 (1999).

[42] T. Basché, W. E. Moerner, M. Orrit, and H. Talon, "Photon antibunching in the fluorescence of a single dye molecule trapped in a solid," Phys. Rev. Lett. **69**, 1516–1519 (1992).

[43] P. Michler, A. Imamoglu, M. D. Mason, P. J. Carson, G. F. Strouse, and S. K. Buratto, "Quantum correlation among photons from a single quantum dot at room temperature," Nature **406**, 968–970 (2000).

[44] C. Santori, D. Fattal, J. Vuckovic, G. S. Solomon, and Y. Yamamoto, "Indistinguishable photons from a single-photon device," Nature **419**, 594–597 (2002).

[45] C. Kurtsiefer, S. Mayer, P. Zarda, and H. Weinfurter, "Stable solid-state source of single photons," Phys. Rev. Lett. **85**, 290–293 (2000).

[46] A. Tribu, G. Sallen, T. Aichele, R. Andre, J.-P. Poizat, C. Bougerol, S. Tatarenko, and K. Kheng, "A high-temperature single-photon source from nanowire quantum dots," Nano Lett. **8**, 4326–4329 (2008).

[47] R. Kolesov, K. Xia, R. Reuter, R. Stöhr, A. Zappe, J. Meijer, P. Hemmer, and J. Wrachtrup, "Optical detection of a single rare-earth ion in a crystal," Nat. Commun. **3**, 1029 (2012).

[48] C. Santori, F. D., and Y. Yamamoto, *Single Photon Device and Applications* (Wiley, 2010).

[49] J. Fan, H. Li, J. Jiang, L. K. Y. So, Y. W. Lam, and P. K. Chu, "3c-sic nanocrystals as fluorescent biological labels," Small **4**, 1058–1062 (2008).

[50] B. Mognetti, A. Barberis, S. Marino, F. Di Carlo, V. Lysenko, O. Marty, and A. Géloën, "Preferential killing of cancer cells using silicon carbide quantum dots," J. Nanosci. Nanotechnol. **10**, 7971–7975 (2010).

[51] T. Serdiuk, V. Lysenko, B. Mognetti, V. Skryshevsky, and A. Géloën, "Impact of cell division on intracellular uptake and nuclear targeting with fluorescent sic-based nanoparticles," J. Biophotonics **6**, 291–297 (2013).

[52] D. Dai, X. Guo, and J. Fan, "Identification of luminescent surface defect in SiC quantum dots," Appl. Phys. Lett. **106**, 053115 (2015).

[53] X. L. Wu, J. Y. Fan, T. Qiu, X. Yang, G. G. Siu, and P. K. Chu, "Experimental evidence for the quantum confinement effect in 3*c*-sic nanocrystallites," Phys. Rev. Lett. **94**, 026102 (2005).

[54] J. Botsoa, V. Lysenko, A. Geloen, O. Marty, J. M. Bluet, and G. Guillot, "Application of 3C-SiC quantum dots for living cell imaging," Appl. Phys. Lett. **92**, 173902 (2008).

[55] D. Beke, Z. Szekrényes, I. Balogh, M. Veres, É. Fazakas, L. K. Varga, K. Kamarás, Z. Czigány, and A. Gali, "Characterization of luminescent silicon carbide nanocrystals prepared by reactive bonding and subsequent wet chemical etching," Appl. Phys. Lett. **99**, 213108 (2011).

[56] S. Yang, B. Kiraly, W. Y. Wang, S. Shang, B. Cao, H. Zeng, Y. Zhao, W. Li, Z.-K. Liu, W. Cai, and T. J. Huang, "Fabrication and characterization of beaded sic quantum rings with anomalous red spectral shift," Adv. Mater. **24**, 5598–5603 (2012).

[57] D. Beke, Z. Szekrényes, D. Pálfi, G. Róna, I. Balogh, P. A. Maák, G. Katona, Z. Czigány, K. Kamarás, B. Rózsa, L. Buday, B. Vértessy, and A. Gali, "Silicon carbide quantum dots for bioimaging," J. Mater. Res. **FirstView**, 1 (2012).

[58] A. Gruber, A. Dräbenstedt, C. Tietz, L. Fleury, J. Wrachtrup, and C. von Borczyskowski, "Scanning confocal optical microscopy and magnetic resonance on single defect centers," Science **276**, 2012 (1997).

[59] V. A. Soltamov, A. A. Soltamova, P. G. Baranov, and I. I. Proskuryakov, "Room temperature coherent spin alignment of silicon vacancies in 4*h*- and 6*h*-sic," Phys. Rev. Lett. **108**, 226402 (2012).

[60] D. Riedel, F. Fuchs, H. Kraus, S. Väth, A. Sperlich, V. Dyakonov, A. A. Soltamova, P. G. Baranov, V. A. Ilyin, and G. V. Astakhov, "Resonant addressing and manipulation of silicon vacancy qubits in silicon carbide," Phys. Rev. Lett. **109**, 226402 (2012).

[61] P. L. Stanwix, L. M. Pham, J. R. Maze, D. Le Sage, T. K. Yeung, P. Cappellaro, P. R. Hemmer, A. Yacoby, M. D. Lukin, and R. L. Walsworth, "Coherence of nitrogen-vacancy electronic spin ensembles in diamond," Phys. Rev. B **82**, 201201 (2010).

[62] I. G. Ivanov, M. Yazdanfar, B. Lundqvist, J.-T. Chen, J. Hassan, P. Stenberg, R. Liljedahl, N. T. Son, J. W. Ager, III, O. Kordina, and E. Janzén, "High-Resolution Raman and Luminescence Spectroscopy of Isotope-Pure(SiC)-Si-28-C-12, Natural and C-13 - Enriched 4H-SIC," (TRANS TECH PUBLICATIONS LTD, 2014) pp. 471–474.

[63] L.-P. Yang, C. Burk, M. Widmann, S.-Y. Lee, J. Wrachtrup, and N. Zhao, "Electron spin decoherence in silicon carbide nuclear spin bath," Phys. Rev. B **90**, 241203 (2014).

[64] F. Zhao, M. M. Islam, and C.-F. Huang, "Photoelectrochemical etching to fabricate single-crystal sic {MEMS} for harsh environments," Mater. Lett. **65**, 409–412 (2011).

[65] M. M. Islam, C.-F. Huang, and F. Zhao, "Single-crystal sic resonators by photoelectrochemical etching," Mater. Sci. Forum **717-720**, 529–532 (2012).

[66] L. Di Cioccio, Y. Le Tiec, F. Letertre, C. Jaussaud, and M. Bruel, "Silicon carbide on insulator formation using the smart cut process," Electron. Lett. **32**, 1144–1145 (1996), .

[67] B.-S. Song, S. Noda, T. Asano, and Y. Akahane, "Ultra-high-q photonic double-heterostructure nanocavity," Nat. Mater. **4**, 207–210 (2005).

[68] K. J. Vahala, "Optical microcavities," Nature **424**, 839–846 (2003).

[69] T. J. Kippenberg and K. J. Vahala, "Cavity optomechanics: Back-action at the mesoscale," Science **321**, 1172–1176 (2008).

[70] J. L. O'Brien, A. Furusawa, and J. Vučković, "Photonic quantum technologies," Nat. Photonics **3**, 687 (2009).

[71] I. J. Wu and G. Y. Guo, "Second-harmonic generation and linear electro-optical coefficients of sic polytypes and nanotubes," Phys. Rev. B **78**, 035447 (2008).

[72] S. Singh, J. R. Potopowicz, L. G. V. Uitert, and S. H. Wemple, "Nonlinear optical properties of hexagonal silicon carbide," Appl. Phys. Lett. **19**, 53 (1971).

[73] P. M. Lundquist, W. P. Lin, G. K. Wong, M. Razeghi, and J. B. Ketterson, "Second harmonic generation in hexagonal silicon carbide," Appl. Phys. Lett. **66**, 1883 (1995).

[74] S. Niedermeier, H. Schillinger, R. Sauerbrey, B. Adolph, and F. Bechstedt, "Second-harmonic generation in silicon carbide polytypes," Appl. Phys. Lett. **75**, 618 (1999).

[75] H. Sato, M. Abe, I. Shoji, J. Suda, and T. Kondo, "Accurate measurements of second-order nonlinear optical coefficients of 6h and 4h silicon carbide," J. Opt. Soc. Am. B **26**, 1892–1896 (2009).

[76] S. Wang, M. Zhan, G. Wang, H. Xuan, W. Zhang, C. Liu, C. Xu, Y. Liu, Z. Wei, and X. Chen, "4h-sic: a new nonlinear material for midinfrared lasers," Laser Photonics Rev. **7**, 831–838 (2013).

[77] R. Hristu, S. Stanciu, D. Tranca, A. Matei, and G. Stanciu, "Nonlinear optical imaging of defects in cubic silicon carbide epilayers," Sci. Rep. **4** (2014), 10.1038/srep05258.

[78] F. Fuchs, V. A. Soltamov, S. Väth, P. G. Baranov, E. N. Mokhov, G. V. Astakhov, and V. Dyakonov, "Silicon carbide light-emitting diode as a prospective room temperature source for single photons," Sci. Rep. **3** (2013).

[79] P. Klimov, A. Falk, B. Buckley, and D. D. Awschalom, "Electrically driven spin resonance in silicon carbide color centers," Phys. Rev. Lett. **112**, 087601 (2014).

[80] A. L. Falk, P. V. Klimov, B. B. Buckley, V. Ivády, I. A. Abrikosov, G. Calusine, W. F. Koehl, A. Gali, and D. D. Awschalom, "Electrically and mechanically tunable electron spins in silicon carbide color centers," Phys. Rev. Lett. **112**, 187601 (2014).

[81] S. E. Saddow, in *Silicon Carbide Biotechnology*, edited by S. E. Saddow (Elsevier, Oxford, 2012).

[82] H. Kraus, V. Soltamov, F. Fuchs, D. Simin, A. Sperlich, P. Baranov, G. Astakhov, and V. Dyakonov, "Magnetic field and temperature sensing with atomic-scale spin defects in silicon carbide," Sci. Rep. **4** (2014).

[83] A. Muzha, F. Fuchs, N. V. Tarakina, D. Simin, M. Trupke, V. A. Soltamov, E. N. Mokhov, P. G. Baranov, V. Dyakonov, A. Krueger, and G. V. Astakhov, "Room-temperature near-infrared silicon carbide nanocrystalline emitters based on optically aligned spin defects," Appl. Phys. Lett. **105**, 243112 (2014).